Journal of Inorganic and Organometallic Polymers and Materials (2020) 30:4954–4968
https://doi.org/10.1007/s10904-020-01745-w

AgI Nanoparticles Decorated $Bi_{24}O_{31}Br_{10}$ Nanosheets: An Efficient 0D/2D Z-Scheme Heterojunction Photocatalyst for the Degradation of Rhodamine B

Tingting Ding[1] · Xinyan Xiao[1] · Yi Wang[1] · Mingli Lu[1]

Received: 17 April 2020 / Accepted: 9 September 2020 / Published online: 15 September 2020

Abstract
A novel 0D/2D Z-scheme AgI/$Bi_{24}O_{31}Br_{10}$ photocatalyst was prepared through the simple solvothermal and coprecipitation method, in which AgI nanoparticles were decorated on the surface of $Bi_{24}O_{31}Br_{10}$ nanosheets. The AgI/$Bi_{24}O_{31}Br_{10}$ composites exhibited improved photocatalytic activity for the degradation of rhodamine B (RhB) in comparison with pristine $Bi_{24}O_{31}Br_{10}$ and AgI under simulated sunlight irradiation. Specifically, AB-30 (mass fraction of AgI, 30%) composite exhibited remarkable photocatalytic activity of 97.6% towards RhB degradation under 120 min of simulated sunlight irradiation, and its RhB degradation rate constant (k) was approximately 20.7 and 2.9 times higher than that of pure $Bi_{24}O_{31}Br_{10}$ and AgI, respectively. The improvement of photocatalytic performance of as-prepared AgI/$Bi_{24}O_{31}Br_{10}$ heterojunction composites was ascribed to the synergistic effect of wide visible-light harvest capacity and the rapid transfer and separation efficiency of charge carriers. UV–vis diffuse reflectance spectra (DRS) analysis validated that the introduction of AgI could broaden the visible-light absorption of AgI/$Bi_{24}O_{31}Br_{10}$ composite. The results of electrochemical impedance (EIS), photocurrent response and photoluminescence spectra (PL) tests showed that AgI/$Bi_{24}O_{31}Br_{10}$ composite possessed the efficient separation and migration of photogenerated charge carriers. Trapping experiments of free radicals certified that $\cdot O_2^-$ was the main reactive species in the process of degradation. And a probable photocatalytic mechanism of Z-scheme heterojunction between $Bi_{24}O_{31}Br_{10}$ and AgI was proposed.

Keywords AgI/$Bi_{24}O_{31}Br_{10}$ · 0D/2D heterostructure · Z-scheme heterojunction · Photocatalytic degradation

1 Introduction

Recently, water contamination associated with organic pollutants has received great concern because of its adverse effects on environment problems and human health [1–3]. Therefore, the effective solution of water pollution is great significance to social development. Luckily, Photocatalytic technology with the advantages of low cost, environment friendly and no secondary pollution is recognized as one of the most effective way to remove organic pollutants [4–6].

Recently, Bi-based photocatalytic materials with suitable band structure, high stability and good visible light response has attracted much attention in the field of photocatalysis, such as Bismuth halide BiOX (X = Cl, Br, I) [7–9], $BiVO_4$ [10] and Bi_2WO_6 [11]. Among them, $Bi_{24}O_{31}Br_{10}$ as a novel photocatalyst with excellent two-dimensional layered structure, high catalytic activity and good stability [12–15]. While the photocatalytic performance of pure semiconductor is inhibited because of the fast combination of charge carriers. Construction of heterojunction photocatalysts has been proven as an advisable strategy to promote the photocatalytic activity of pure $Bi_{24}O_{31}Br_{10}$ [16, 17]. Wu and his co-workers reported WO_3/$Bi_{24}O_{31}Br_{10}$ composite via a hydrothermal method, and exhibited prominent visible-light degradation activity for removing tetracycline (TC) [18]. Peng et al. constructed $Bi_{12}O_{17}Br_2$/$Bi_{24}O_{31}Br_{10}$ type II heterojunction with excellent photocatalytic activity for the degradation of RhB due to the improved separation of photogenerated carriers [19]. Compared with conventional type II heterojunction, Z-scheme heterojunction photocatalyst may represents better photocatalytic activity, which was ascribed to efficient

✉ Xinyan Xiao
cexyxiao@scut.edu.cn

[1] School of Chemistry and Chemical Engineering, Guangdong Provincial Key Lab of Green Chemical Product Technology, South China University of Technology, Guangzhou 510640, China

separation efficiency of carriers and strong redox potential [20]. He et al. reported AgBr/$Bi_{24}O_{31}Br_{10}$ Z-scheme photocatalysts have excellent photocatalytic property and stability, which could be ascribed to enhancement of visible-light harvest capability, separation efficiency of carriers and redox capacity [21]. Xue et al. fabricated a novel g-C_3N_4/Bi_2WO_6/AgI heterojunction via hydrothermal and in-situ precipitation process, and the samples exhibited extraordinary photocatalytic activity for removal of TC, which benefited from the formation of direct dual Z-scheme structure [22].

Silver iodide (AgI) is a photosensitive semiconductor with good visible light response and suitable band structure (~2.7 eV) [23]. However, AgI is easy to aggregate and suffer from photo-corrosion, resulting in the reduction of its specific surface area, photocatalytic activity and stability [24]. To address above drawbacks of pure AgI, constructing heterojunction photocatalyst is a promising strategy, including BiOI/Ag@AgI [25], AgI/BiOBr [26], AgI/Bi_2WO_6 [27] and AgI/BiOBr/RGO [28]. Besides, designing unique heterostructure, such as 0D/2D, 1D/2D and 2D/2D structure, could reduce the transfer distance of carriers in the heterojunction interface and enhance the absorption capacity of visible-light, resulting in superior photocatalytic activity and stability [29]. Thus, construction of AgI/$Bi_{24}O_{31}Br_{10}$ 0D/2D Z-scheme system is an effective strategy to facilitate the carriers separation efficiency, increase the response of visible-light and improve the photocatalytic property.

In this work, a novel Z-scheme AgI/$Bi_{24}O_{31}Br_{10}$ 0D/2D photocatalyst was constructed by simple methods of solvothermal and coprecipitation. The structure and morphology of samples were investigated by X-ray diffractometer (XRD), field emission scanning electron microscope (SEM) and transmission electron microscope (TEM). And the optical properties, charge-transfer properties and photoelectrochemical properties were investigated by Mott-Schottky method (M-S), PL, EIS and photocurrent response tests. The photocatalytic activities and recyclability of AgI/$Bi_{24}O_{31}Br_{10}$ composites were evaluated by photodegradation of RhB under simulated sunlight irradiation. Additionally, combined with the result of DRS analysis and trapping experiments of free radicals, a probable photocatalytic mechanism of Z-scheme heterojunction between $Bi_{24}O_{31}Br_{10}$ and AgI was proposed.

2 Experimental

2.1 Materials

Bismuth nitrate pentahydrate ($Bi(NO_3)_3{\cdot}5H_2O$), silver nitrate ($AgNO_3$) were purchased from Aladdin Chemistry Co., Ltd. Potassium bromide (KBr) and ethylene glycol (EG) were obtained from Sinopharm Chemical Reagent Co., Ltd. Ethanol amine was supplied by Shanghai Macklin Biochemical Co., Ltd.

2.2 Preparation of AgI/$Bi_{24}O_{31}Br_{10}$ Heterojunction

$Bi_{24}O_{31}Br_{10}$ was synthesized through a simple solvothermal method [30]. Briefly, 1.94 g of $Bi(NO_3)_3{\cdot}5H_2O$ was dissolved into 20 mL of EG and stirred for 30 min to form a transparent solution, labeled solution A. Meanwhile, 1.2 g of KBr was dispersed into 50 mL deionized water to form solution B. And then, solution B was slowly dropped into solution A and kept stirring for 10 min. Subsequently, 2.4 mL of ethanol amine was dropwise added into resulting suspension and stirred for 20 min. The white homogeneous suspension was transferred into a 100 mL Teflon-lined autoclave, maintained at 160 °C for 12 h. After that, the obtained yellow product was centrifuged, washed, and then dried at 60 °C overnight.

The AgI/$Bi_{24}O_{31}Br_{10}$ composite was synthesized by a coprecipitation process (Fig. 1). Firstly, 0.2 g of as-prepared $Bi_{24}O_{31}Br_{10}$ was dispersed into 30 mL of deionized water and ultrasonicated for 15 min. After that, determined amount of KI was added into the dispersed solution under stir treatment for 30 min. Subsequently, 20 mL $AgNO_3$ solution, containing a certain amount of $AgNO_3$ (the molar ratio of Ag^+: I^- = 1: 1), was dropwise added to the above uniform suspension and kept stirring for 2 h in the dark. Finally, the resulting product was collected, washed and then dried at 60 °C overnight. The obtained composites of different theoretical mass ratios of AgI with 10%, 20%, 30% and 35%, were marked as AB-10, AB-20, AB-30 and AB-35, respectively. For comparison, the pristine AgI was also prepared under the similar conditions but without the addition of $Bi_{24}O_{31}Br_{10}$.

2.3 Characterization

The samples of structures were recorded in a rage of 5°-70° on an X-ray diffractometer (XRD, D8 ADVANCE) with Cu Ka radiation. The morphology and structure of as-obtained materials were analyzed by a field emission scanning electron microscope, energy dispersive X-ray spectroscope analysis (SEM, EDX mapping, Hitachi SU8220) and transmission electron microscope (TEM, JEM-2010, Japan). Zeta potentials were measured by a nanoparticle analyzer (HORIBA, SZ-100). The UV–vis DRS were investigated by a UV–vis spectrometer (Hitachi, UV-3010) to investigate the optical performances, using $BaSO_4$ as a reference standard. X-ray photoelectron spectroscopy (XPS) was measured on a Thermo Fisher Scientific K-Alpha XPS instrument to analyze the surface properties. A Micromeritics ASAP 2460 3.01 analyzer was applied to estimate the Brunauer–Emmett–Teller specific surface area (S_{BET}).

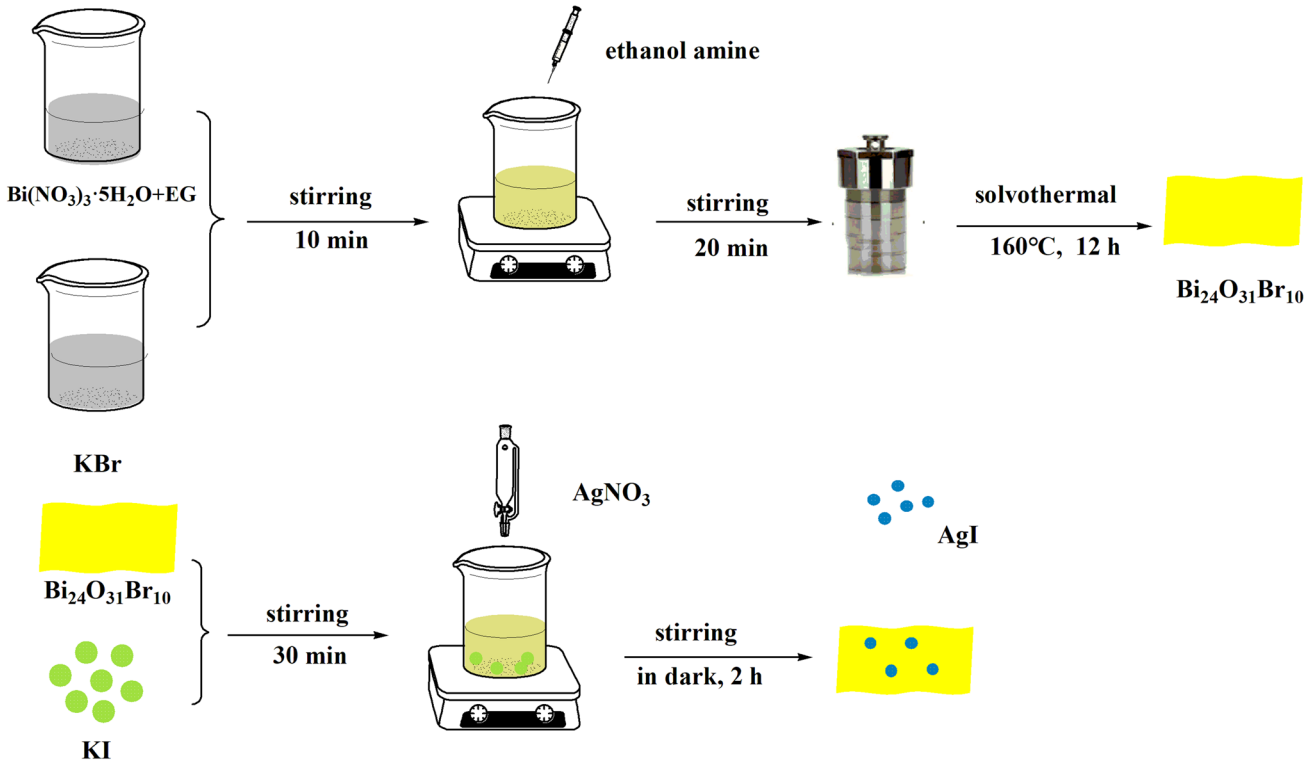

Fig. 1 Schematic illustration for the synthesis of AgI/$Bi_{24}O_{31}Br_{10}$ composite

Photoluminescence (PL) spectra were monitored using a fluorescence spectrometer (Hitachi F-4500). The photocurrent density and electrochemical and impedance (EIS) were completed on electrochemical workstation (Chenhua CHI-660C, Shanghai) with a typical three-electrode system to study charge-transfer properties.

2.4 Photocatalytic Measurements

To estimate the photocatalytic activities of AgI, $Bi_{24}O_{31}Br_{10}$ and AgI/$Bi_{24}O_{31}Br_{10}$ composites, photodegradation of RhB were implemented under simulated sunlight irradiation (a 500 W Xe arc lamp (XG500) and the illumination power was 32 mW/cm^2 measured by optical power meter (PL-MW2000)). In detail, 50 mg of the obtained catalyst samples were severally dispersed into 100 mL of RhB solution (10 mg L^{-1}) and kept stirring in dark for 30 min to obtain the adsorption–desorption equilibrium. The concentration change of RhB solution was detected by the maximum absorbance at 553 nm using a spectrophotometer (Shimadzu, UV-3600). The degradation efficiency (η) of RhB could be calculated according to the Eq. (1):

$$\eta(\%) = \left[\left(C_0 - C_t\right)/C_0\right] \times 100\% \quad (1)$$

where C_t and C_0 represented the concentration of RhB solution at reaction time t and initial concentration, respectively.

The degradation efficiency and cycling stability of RhB were studied through three experiments and the standard deviation (S) of the results could be calculated according to the Eq. (2).

$$S = \sqrt{\frac{\sum_{i=1}^{n}\left(x_i - \bar{x}\right)}{n}} \quad (2)$$

where x_i, $\bar{x}$ and n represented a certain number, the average value and number of a set of data, respectively.

2.5 Recycling Experiments

The recycling experiments of the photocatalysts for contaminants degradation were performed in the similar condition. After each photocatalytic reaction, the supernatant was poured off, the remaining catalysts were collected and washed several times with deionized water and absolute alcohol, then dried at 60 °C for 12 h and weighted. Then the used photocatalysts were suspended into fresh contaminant solution again and experiment was repeated for four times.

2.6 Photoelectrochemical Measurements

Photoelectrochemical measurements were conducted on an electrochemical station (Chenhua CHI-660C, Shanghai) with a three-electrode system. A platinum sheet was adopted as the counter electrode and Ag/AgCl electrode was employed as reference electrode, respectively. And 0.5 M sodium sulfate (Na_2SO_4) was served as electrolyte. The working electrode was a film electrode, preparing as the following method: 10 mg of photocatalyst and 40 µL of Nafion solution were dispersed into 1 mL of absolute ethanol. After scattering, 0.2 mL of the suspension was dropped on the surface of FTO with an effective area of 1 cm × 1 cm and then dried at 60 °C for 5 h.

3 Results and Discussion

3.1 Characterization

The XRD patterns of pure $Bi_{24}O_{31}Br_{10}$, AgI and AgI/$Bi_{24}O_{31}Br_{10}$ composites were exposed in Fig. 2. Several representative diffraction peaks of $Bi_{24}O_{31}Br_{10}$ at 10.52°, 23.73°, 25.05°, 29.76°, 31.82°, 39.98° and 54.62° can be correspond to the (102), (008), (206), (213), (117), (011) and (324) crystal facets of monoclinic $Bi_{24}O_{31}Br_{10}$ (PDF#75–0888), respectively [16]. The unique diffraction peaks of pristine AgI at $2\theta = 22.4°$, 23.8°, 39.3° and 46.5° are correspond to (100), (111), (220) and (311) planes of AgI, respectively, which can be well indexed to hexagonal plane of AgI phase (PDF#09–0399) [31]. With respect to the AgI/$Bi_{24}O_{31}Br_{10}$ composites, the characteristic diffraction peaks of pure monoclinic $Bi_{24}O_{31}Br_{10}$ and hexagonal AgI can be detected,

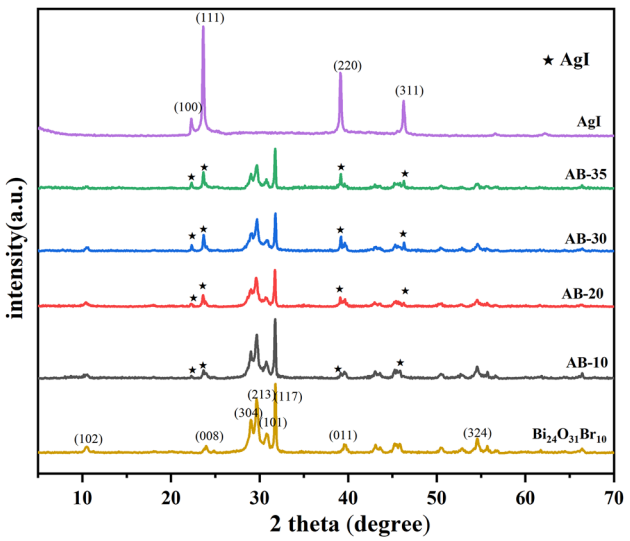

Fig. 2 XRD patterns of $Bi_{24}O_{31}Br_{10}$, AgI and AB-x samples

declaring successful preparation of AgI/$Bi_{24}O_{31}Br_{10}$ composite. Furthermore, it is clearly observed that the intensities of AgI special diffraction peaks at $2\theta = 22.4°$, 23.8°, 39.3° increase gradually with the increase of the mass fraction of AgI in the patterns of AgI/$Bi_{24}O_{31}Br_{10}$ composites. While the characteristic diffraction peaks of $Bi_{24}O_{31}Br_{10}$ are weaken. Meanwhile, no other impurity diffraction peaks are observed, suggesting that AgI/$Bi_{24}O_{31}Br_{10}$ composites possess a high purity composite constructed of AgI and $Bi_{24}O_{31}Br_{10}$.

The morphology of $Bi_{24}O_{31}Br_{10}$, AgI and AB-30 composite was observed by SEM. As shown in Fig. 3a, b, the pristine $Bi_{24}O_{31}Br_{10}$ shows irregular nanosheets with thickness of about 20–30 nm. The morphology of pristine AgI shows irregular and agglomerated particles with diameters of 2–3 µm in Fig. 3c. As for AB-30 composite (Fig. 3d), it can be clearly observed that 0D AgI particles are successfully scattered over 2D $Bi_{24}O_{31}Br_{10}$ nanosheets, certificating the formation of 0D/2D nanostructure. Notably, the diameter of AgI particles located on the surface of $Bi_{24}O_{31}Br_{10}$ is much smaller than pristine AgI particles. And the size of AgI particles in AB-30 composite are significantly reduced to about 30–40 nm in diameter because $Bi_{24}O_{31}Br_{10}$ with large specific surface area is conductive to the dispersion and inhibition the self-aggregating of AgI [32].

As displayed in TEM image of AB-30 composite (Fig. 4a), AgI nanoparticles closely locate on the surface of $Bi_{24}O_{31}Br_{10}$ nanosheets, which is consistent with SEM. As revealed in the HRTEM (Fig. 4b), There are two types of the interplanar lattice distance at 0.29 and 0.23 nm, corresponding to the (213) crystal facet of $Bi_{24}O_{31}Br_{10}$ and (220) crystal facet of AgI, respectively. According to the EDX mapping image of AB-30 composite (Fig. 4c–h), the elements of Br, O, Bi, Ag and I are evenly distributed on the surface of AB-30 composite, demonstrating AgI is successfully coupled with $Bi_{24}O_{31}Br_{10}$. The results of SEM, TEM and EDX mapping analysis certify that the formation of unique 0D/2D heterostructure in the AB-30 composite, which is conducive to increasing the dispersion of AgI nanoparticles, exposing more active sites, and therefore enhanced the photodegradation performance of coupling system.

The element compositions and chemical states of the AgI, $Bi_{24}O_{31}Br_{10}$, AB-30 composite were investigated by X-ray photoemission spectroscopy (XPS). Based on the XPS results of $Bi_{24}O_{31}Br_{10}$ and AB-30 composite, there exist the elements of Bi, Br and O. In addition, the binding energy of I 3d and Ag 3d are detected in AB-30 composite, indicating the existence of AgI in the AB-30 composite (Fig. 5a). The Bi 4f binding energy (Fig. 5b) peaks located at 159.41 eV and 164.7 eV are correspond to Bi $4f_{7/2}$ and Bi $4f_{5/2}$, respectively, which implies that the chemical state of element Bi is Bi^{3+} in the $Bi_{24}O_{31}Br_{10}$ [33]. In Fig. 5c, the peaks of $Bi_{24}O_{31}Br_{10}$ at 68.58 eV and 69.64 eV belong

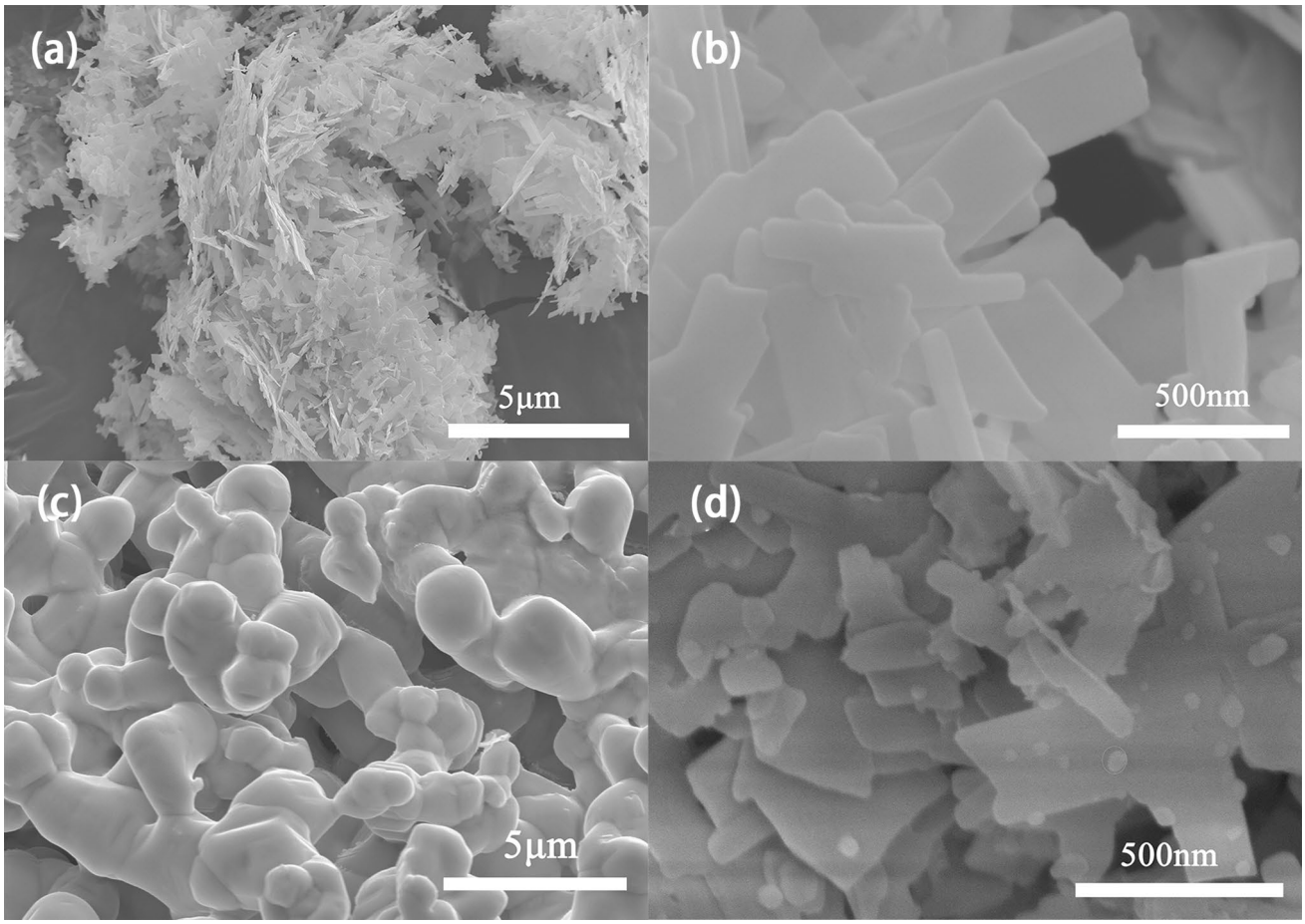

Fig. 3 SEM images of **a, b** $Bi_{24}O_{31}Br_{10}$, **c** AgI, **d** AB-30 composite

to Br $3d_{5/2}$ and Br $3d_{3/2}$, respectively [34]. And the O 1 s peaks at 530.1 eV and 531.7 eV belong to Bi-O in the form of $[Bi_2O_2]^{2+}$ and H–O in $Bi_{24}O_{31}Br_{10}$ and AB-30 composite [32], respectively (Fig. 5d). For AgI, the peaks at 619.7 eV and 631.17 eV in Fig. 5e are assigned to I $3d_{5/2}$ and I $3d_{3/2}$, respectively [35]. Similarly, the XPS spectra at 368.44 eV and 374.42 eV in Fig. 5f are separately assigned to $3d_{5/2}$ and $3d_{3/2}$ of Ag, which represents the Ag^+ in AgI [36]. Notably, the I 3d and Ag 3d of binding energy for AB-30 composite show a slight negative shift compared to pure AgI, while the Br 3d of binding energies display a slight positive shift compared to bare $Bi_{24}O_{31}Br_{10}$, which could be ascribed to the partial electron transfer from $Bi_{24}O_{31}Br_{10}$ to AgI. This would increase the electron density of AgI, leading to reduction in the binding energy of I 3d and Ag 3d. On the contrary, the electron density of $Bi_{24}O_{31}Br_{10}$ decreases, resulting in enhancement of binding energy of Br 3d [18, 37]. Simultaneously the characteristic binding energies of Ag^0 is not detected, proving that there is no metallic Ag in AB-30 composite [38]. The results of XPS were consistent with EDX, SEM and TEM, indicating that AB composite was successfully prepared.

The consequences of S_{BET} and the corresponding pore size distribution of pristine $Bi_{24}O_{31}Br_{10}$, AgI and AB-30 composite by N_2 adsorption–desorption isotherms are shown in Fig. 6. The curves of samples conform to the type IV isotherms with a hysteresis, formed by the aggregation of sheet particles or fragmented porous materials, indicating the presence of mesopores [37, 39]. The S_{BET}, the average pore volume and BJH pore diameter distributions of $Bi_{24}O_{31}Br_{10}$, AgI and AB-30 composite are presented in Table 1. And the S_{BET} of $Bi_{24}O_{31}Br_{10}$ is 15.58 $m^2\ g^{-1}$, the S_{BET} of AgI is 1.07 $m^2\ g^{-1}$, and that of AB-30 composite is 10.12 $m^2\ g^{-1}$ because of the introduction of AgI nanoparticles [40].

The optical properties of AgI, $Bi_{24}O_{31}Br_{10}$ and AB-30 composite were measured through UV–vis spectra (Fig. 7a). It can be clearly observed that the absorption edges of pure $Bi_{24}O_{31}Br_{10}$ and AgI are approximately at 510 and 450 nm, respectively. Strikingly, the absorption strength of AB-30 composite in the visible region is higher than that of pure

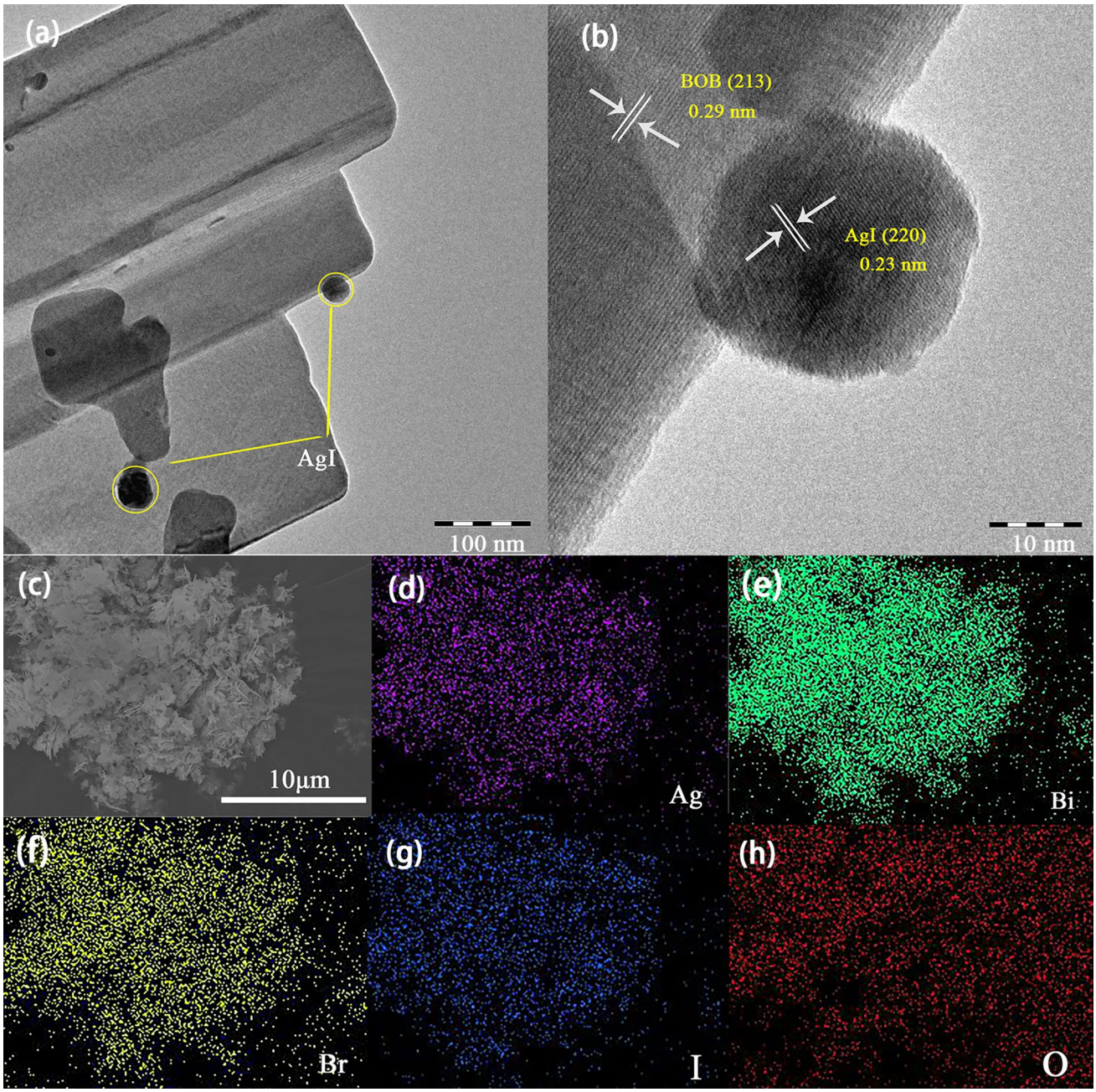

Fig. 4 TEM (**a**), HRTEM (**b**) and EDX mapping (**c–h**) images of AB-30 composite

$Bi_{24}O_{31}Br_{10}$ and AgI, which could be ascribe to the reflection of light in the 0D/2D hierarchical structure [41]. In general, the band gap (E_g) of $Bi_{24}O_{31}Br_{10}$ and AgI can be calculated by following Eq. (3) [42]:

$$\alpha h\nu = A\left(h\nu - E_g\right)^{n/2} \tag{3}$$

where α, ν, A, h, and E_g are absorption coefficient, light frequency, constant, Planck constant and bandgap, respectively. n depends on the transition properties of the semiconductor. For $Bi_{24}O_{31}Br_{10}$ and AgI, n values are severally equal to 4 and 1 [30]. With $(\alpha h\nu)^{1/2}$ and $(\alpha h\nu)^2$ as the Y-axis, respectively, $h\nu$ plotted as the X-axis and the results are shown in Fig. 7b and c, the E_g of $Bi_{24}O_{31}Br_{10}$ and AgI are 2.25 eV and 2.78 eV, respectively.

The flat band potential (E_f) of $Bi_{24}O_{31}Br_{10}$ and AgI are measured by Motte-Schottky (M-S) plots. The slope of M-S curve for $Bi_{24}O_{31}Br_{10}$ is negative, indicating that it is p-type semiconductor, and vice versa AgI belongs to n-type semiconductor [43]. As for the n-type semiconductor, the

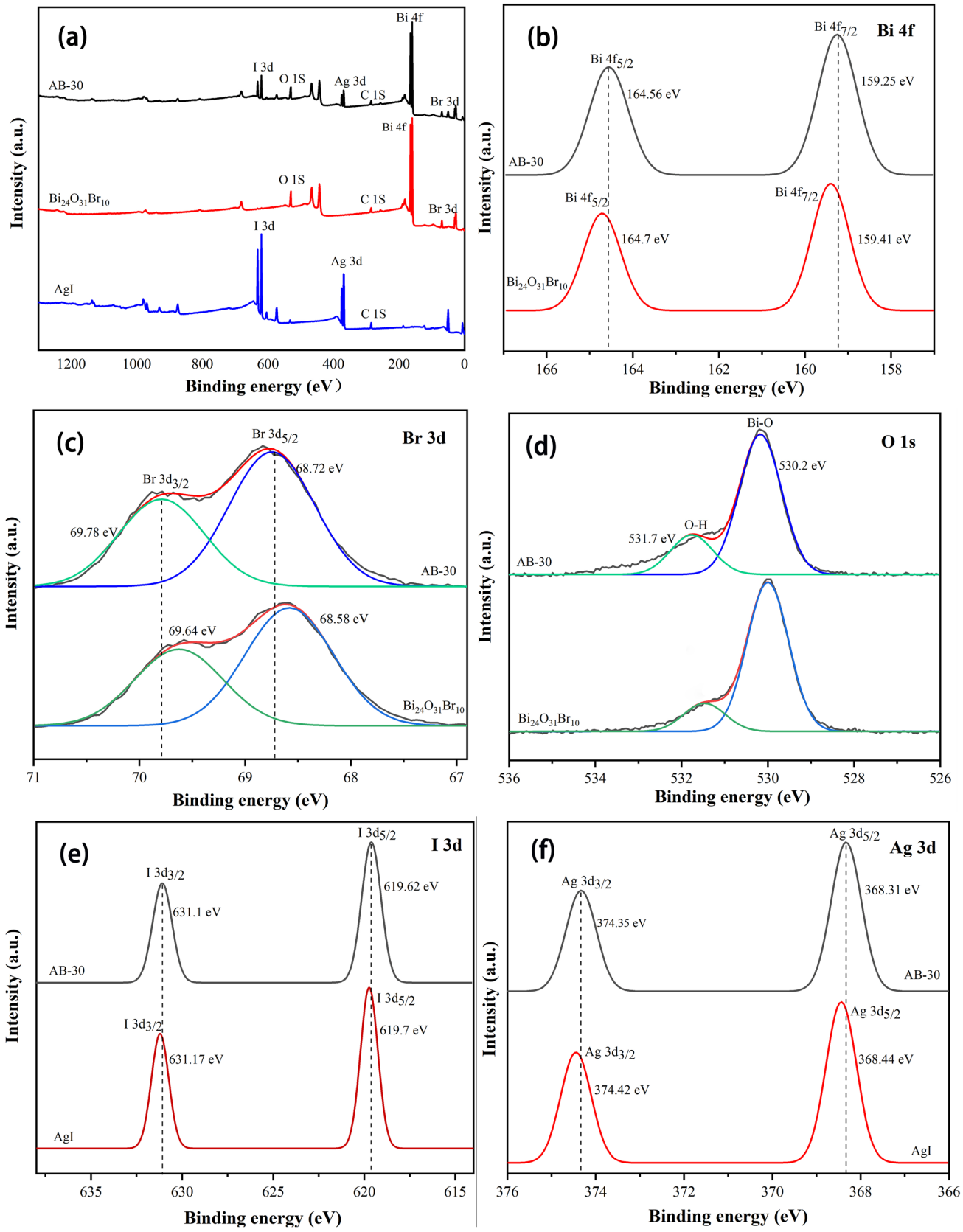

Fig. 5 XPS spectra of the AB-30 composite; **a** Survey of the sample; **b** Bi 4f, **c** Br 3d, **d** I 3d, **e** O 1 s and **f** Ag 3d

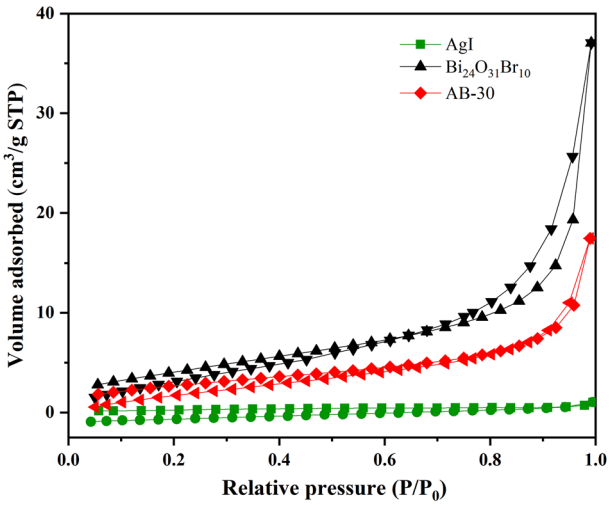

Fig. 6 Nitrogen adsorption–desorption isotherms of $Bi_{24}O_{31}Br_{10}$, AgI and AB-30 composite

Table 1 S_{BET}, average pore volume and pore diameter of $Bi_{24}O_{31}Br_{10}$, AgI and AB-30 composite

Sample	V_{pore} ($cm^3\ g^{-1}$)	D_{pore} (nm)	S_{BET} ($m^2\ g^{-1}$)
$Bi_{24}O_{31}Br_{10}$	0.057	13.50	15.58
AgI	0.0016	16.20	1.070
AB-30	0.027	11.17	10.12

E_f is approximately equal to its CB potential (E_{CB}), while the E_f of the p-type semiconductor is about equal to its VB potential (E_{VB}). Therefore, the E_{VB} of $Bi_{24}O_{31}Br_{10}$ and E_{CB} of AgI are about 2.7 V and −0.6 V vs. Ag/AgCl electrode (Fig. 8a, b), and then corresponding to 2.9 V and −0.4 V vs. the standard hydrogen electrode, respectively. Moreover, The E_{CB} of $Bi_{24}O_{31}Br_{10}$ and E_{VB} of AgI can be calculated using the following Equation [44]:

$$E_{CB} = E_{VB} - E_g \tag{4}$$

According to the results of bandgap energy (E_g) obtained by UV–vis DRS spectra, the E_{CB} value of $Bi_{24}O_{31}Br_{10}$ is 0.65 V and the E_{VB} value of AgI is 2.38 V.

3.2 Photocatalytic Performance

The photocatalytic performance of AgI, $Bi_{24}O_{31}Br_{10}$ and AgI/$Bi_{24}O_{31}Br_{10}$ composites were evaluated by analyzing the changes of RhB content with time under simulated sunlight irradiation. As seen in Fig. 9a, the direct photodegradation of RhB without photocatalyst can almost be neglected. The adsorption capacity of the AgI/$Bi_{24}O_{31}Br_{10}$ composites in the dark reaction was higher than that of the pure $Bi_{24}O_{31}Br_{10}$ and AgI, which contributes to the photocatalytic degradation process. Moreover, the Zeta potential for as-prepared samples were performed to further clarify the adsorption behavior, in which the measured mass concentration of all samples is 10 mg/L and the solvent is deionized water. As shown in Fig. 10, the surface of samples are negatively charged and their charge value decrease as follows: AB-30>$Bi_{24}O_{31}Br_{10}$>AgI. Obviously, the results of Zeta potential were consistent with the adsorption capacity of the samples in the dark due to their opposite charge between as-prepared samples and RhB. As for $Bi_{24}O_{31}Br_{10}$, 21.41% of RhB is degraded in 120 min under simulated sunlight irradiation. And 72.23% of RhB is degraded in the presence of AgI under the same conditions. The photocatalytic activity of AgI/$Bi_{24}O_{31}Br_{10}$ composites first gradually increases and then decreases with the increase of AgI content in AgI/$Bi_{24}O_{31}Br_{10}$ composites. Especially, the AB-30 composite exhibits the optimum photocatalytic efficiency with degradation of 97.6% for RhB under identical conditions. Therefore, the proper proportion of AgI and $Bi_{24}O_{31}Br_{10}$ in composite is beneficial to boost the photodegradation activity. The degradation rate constants of as-prepared samples were further studied by a first-order reaction kinetics and the model as follows [45]:

$$-\ln\left(C/C_0\right) = kt \tag{5}$$

where k stands for rate constant, C and C_0 are the concentration of RhB at reaction time t and 0, respectively. As displayed in Fig. 9b and c, the rate constants (k) of RhB degradation are 0.0013, 0.010, 0.0083, 0.013, 0.029 and 0.017 min^{-1} for $Bi_{24}O_{31}Br_{10}$, AgI, AB-10, AB-20, AB-30 and AB-35 composite, respectively. Notably, the AB-30 composite possesses the greatest k (0.029 min^{-1}) with nearly 20.74 times and 2.85 times higher than that of bare $Bi_{24}O_{31}Br_{10}$ and AgI, respectively. Therefore, the photocatalytic performance of $Bi_{24}O_{31}Br_{10}$ modified by AgI can significantly strengthen.

The cyclic stability and reusability of photocatalyst is also an important performance index, especially when the composites contain photosensitive and unstable semiconductor AgI. The photostability of AB-30 composite for RhB decomposition was evaluated via four cycle experiments. It is shown in Fig. 10a that the degradation efficiencies of RhB are 97.60%, 94.84%, 91.37% and 86.43% for 1st, 2nd, 3rd and 4th run, respectively. There is no significant decrease after four recycles of photodegradation process. Furthermore, the XRD patterns and SEM of used and fresh AB-30 composite are implemented to further certify the stability of AB-30 composite. There is no significant difference crystalline phase and morphology change can be observed via XRD patterns and SEM images before and after the photocatalytic

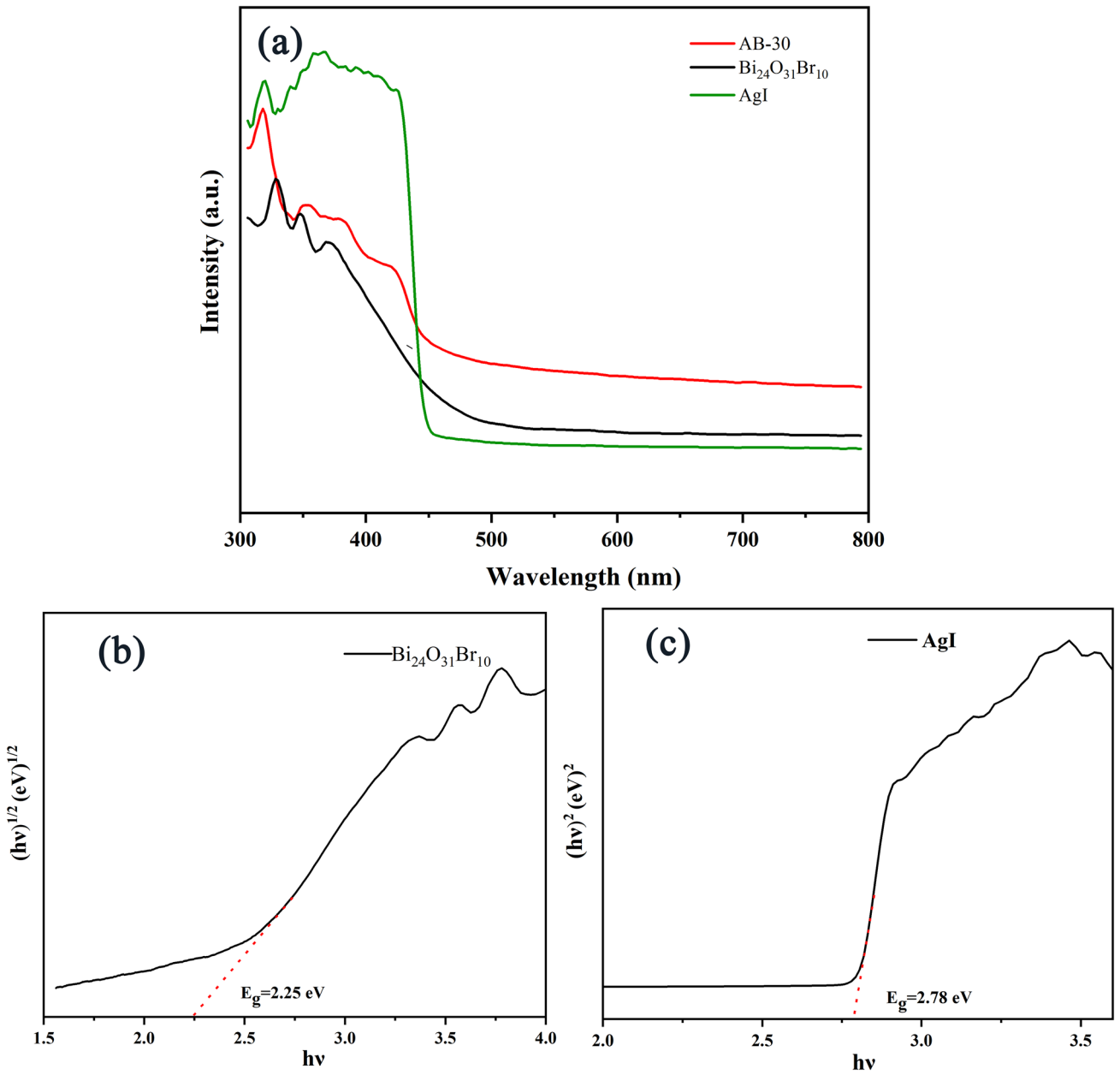

Fig. 7 **a** UV – vis DRS for $Bi_{24}O_{31}Br_{10}$, AgI and AB-30 composite; **b**, **c** The band gaps of $Bi_{24}O_{31}Br_{10}$ and AgI, respectively

tests (Fig. 11b–d), implying that the as-prepared AB-30 composite possesses good reusability and stability.

3.3 Charge-transfer Properties

The charge separation and transfer are also significant factors on photocatalytic activity. Thus, photocurrent response and EIS tests of as-prepared $Bi_{24}O_{31}Br_{10}$ and AB-30 composite were analyzed to study the charge separation and transfer capacity. The photocurrent response of AB-30 composite (~ 0.97 μA/cm^2) is approximately 8 times than that of pristine $Bi_{24}O_{31}Br_{10}$ (~ 0.12 μA/cm^2) in Fig. 12a, which indicates that AB-30 composite has higher separation efficiency of photoinduced electron–hole pairs than pristine $Bi_{24}O_{31}Br_{10}$ and the result is consistent with the degradation activity. Moreover, the EIS of $Bi_{24}O_{31}Br_{10}$ and AB-30 are shown measured in Fig. 12b. The curvature radius of AB-30 composite is much smaller than that of $Bi_{24}O_{31}Br_{10}$, indicating that AB-30 composite has lower interface impedance and higher charge migration efficiency because the smaller curve radius corresponds to the higher electron transfer efficiency and lower impedance in Nyquist plots [46]. The

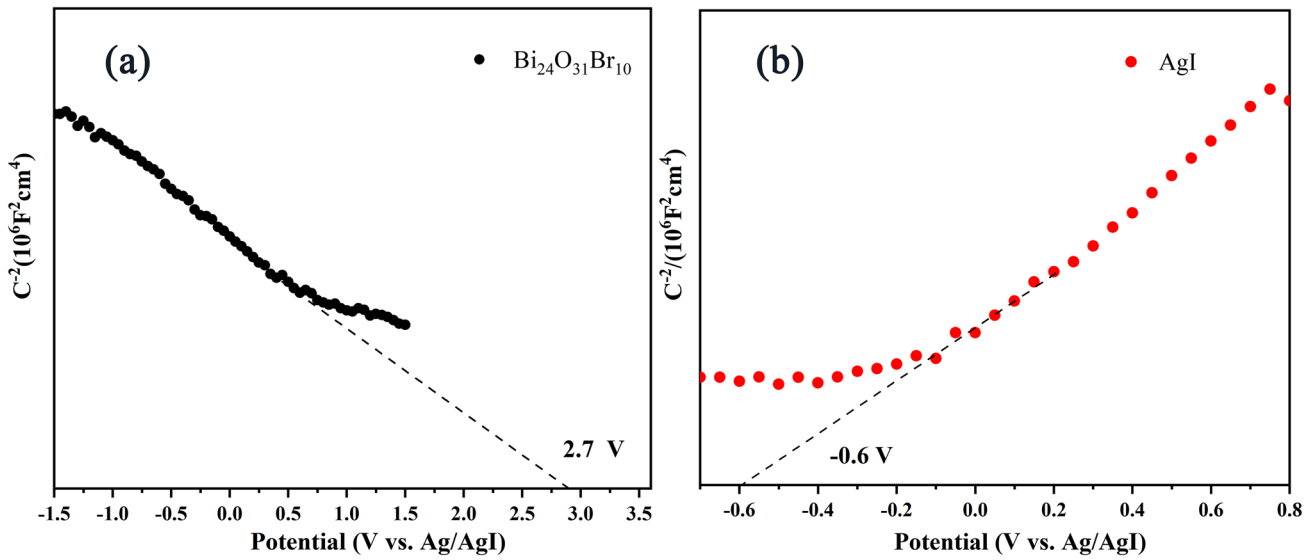

Fig. 8 **a**, **b** Mott-Schottky plots of $Bi_{24}O_{31}Br_{10}$ and AgI, respectively

results of photocurrent responses and EIS are consistent, which further proves that the AB-30 composite possesses higher separation and transfer efficiency of photogenerated carriers compared to pristine $Bi_{24}O_{31}Br_{10,}$ resulting in the enhanced photocatalysis activity.

The photoluminescence spectroscopy (PL) of pristine AgI, $Bi_{24}O_{31}Br_{10}$ and AB-30 composite were recorded to conduct the recombination of photogenerated electrons and holes in the semiconductors with 325 nm excitation wavelength. The strength of PL is proportional to the s recombination of photogenerated carriers. From in Fig. 13, AB-30 composite has the lowest PL intensity, indicating that AB-30 composite possesses the lowest photogenerated charge carriers recombination, benefiting from shorter transfer distance of charge carriers between 0D AgI nanoparticles and 2D $Bi_{24}O_{31}Br_{10}$ nanosheets. This result is consistent with that of photocurrent responses and EIS. Based on the consequences of PL, EIS and photocurrent response, it can conclude that the construction of 0D/2D AB-x composites heterostructure, deposition of AgI on the surface of $Bi_{24}O_{31}Br_{10}$, could effectively boost separation and transfer of photo-excited charge carriers, which is helpful to improve the photocatalytic activity.

3.4 Photocatalytic Mechanism

The trapping experiments were conducted, in which 1,4-benzoquinone (BQ), tert-butyl alcohol (TBA) and ammonium oxalate (AO) are employed as quenchers for $\cdot O_2^-$, ·OH and h^+, respectively (Fig. 14). The photodegradation efficiency of RhB decreased from 97.6% to 7.3% when BQ was added to AB-30 composites, certificating that $\cdot O_2^-$ radicals play a vital role in the process of photocatalysis. Similarly, the degradation efficiency of RhB also distinctly decreased to 51.1% and 70.3% in the presence of AO and TBA, respectively, indicating that h^+ and ·OH radicals play a secondary role.

According to the above analysis, the possible mechanism of RhB photodegradation over AB-x composites was proposed. Known from the results of DRS, both AgI and $Bi_{24}O_{31}Br_{10}$ could be excited to produce electrons and holes under simulated sunlight irradiation. The E_{CB} and E_{VB} values for the $Bi_{24}O_{31}Br_{10}$ are 0.65 V and 2.9 V, while the values of AgI are -0.4 V and 2.38 V, respectively. Both the CB and VB of $Bi_{24}O_{31}Br_{10}$ more positive than that of AgI. If the transfer path of photogenerated electrons and holes follows the traditional type-II heterojunction model (Fig. 15a), the electrons tend to transfer from more negative CB of AgI to CB of $Bi_{24}O_{31}Br_{10}$ and the holes are liable to migrate from the more positive VB of $Bi_{24}O_{31}Br_{10}$ to VB of AgI. However, the electrons accumulated on CB of $Bi_{24}O_{31}Br_{10}$ are unable to react with O_2 to yield $\cdot O_2^-$ because the CB potential of $Bi_{24}O_{31}Br_{10}$ (0.65 V) is more positive than that of $O_2/\cdot O_2^-$ (-0.33 V vs. NHE). Besides, the holes remained on VB of AgI (2.38 V) could not oxidize H_2O to form ·OH because the VB potential of AgI is more negative than that of $H_2O/\cdot OH$ (2.72 V vs. NHE). Therefore, neither $\cdot O_2^-$ nor ·OH could be produced, which contradicted the result of trapping experiments. As a result, the conventional type-II charge transfer mechanism is impractical for AB-x composite over photodegradation RhB. Based on the above discussion, it is more reasonable for Z-scheme mechanism to account for the migration of photogenerated electrons and holes in photodegradation process of RhB (Fig. 15b). The photogenerated

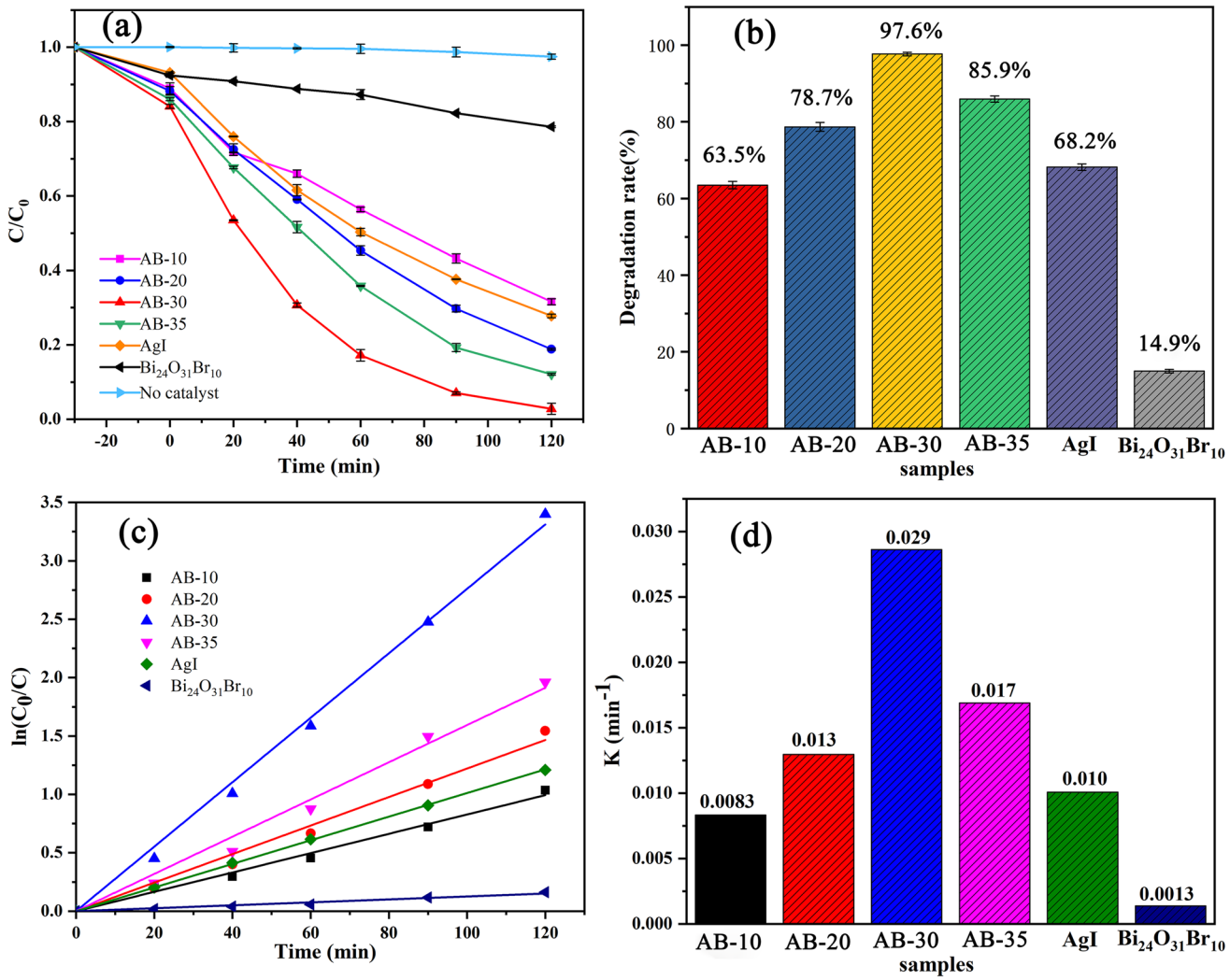

Fig. 9 **a**, **b** Photocatalytic performance of as-prepared samples toward degradation of RhB; **c**, **d** The pseudo-first-order kinetics of RhB degradation

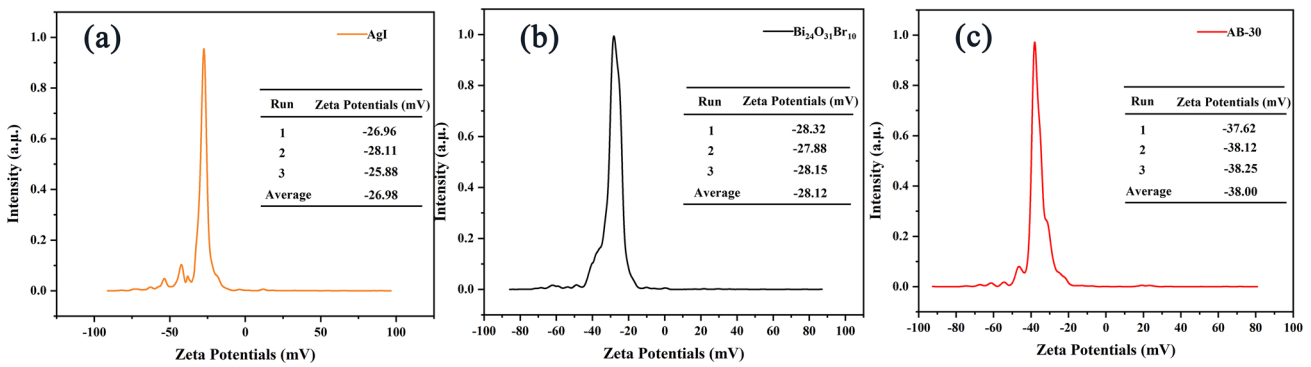

Fig. 10 Zeta potential of AgI (**a**), $Bi_{24}O_{31}Br_{10}$ (**b**), AB-30 (**c**)

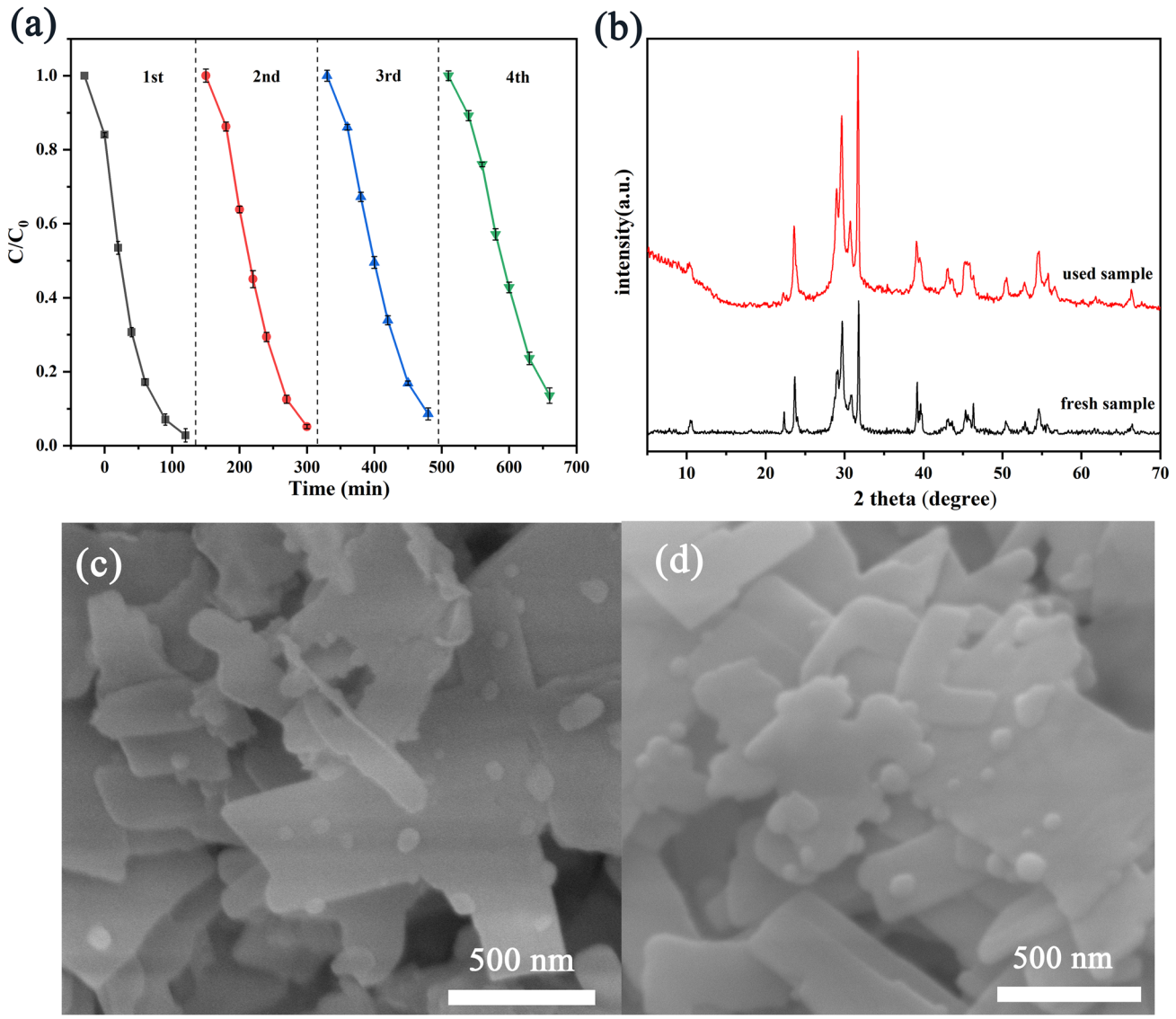

Fig. 11 **a** Cycling runs of AB-30 composite toward degradation of RhB; **b** XRD patterns and **c**, **d** SEM images of AB-30 composite before and after the cycling photocatalytic experiments

electrons in the CB of $Bi_{24}O_{31}Br_{10}$ could recombine with the holes in VB of AgI, and then significantly inhibited the recombination of photogenerated electrons and holes accumulated on AgI and $Bi_{24}O_{31}Br_{10}$. The electrons retaining in CB of AgI could reduce the O_2 absorbed on the surface to form $\cdot O_2^-$ because the electrons in the CB of AgI are more negative than the potential of $O_2/\cdot O_2^-$. And the generated $\cdot O_2^-$ is a vital active specie for degradation of RhB. Meanwhile, the holes accumulated on the VB of $Bi_{24}O_{31}Br_{10}$ could activate H_2O or OH^- to produce ·OH and then ·OH oxidize RhB. In addition, holes in VB of $Bi_{24}O_{31}Br_{10}$ with strong oxidation ability could directly contribute to the degradation of pollutants. Therefore, it can be concluded that the degradation of RhB over AB-x composites is consistent with the Z-scheme mechanism, resulting in efficient separation of photogenerated carriers and enhanced redox capacity.

4 Conclusions

In summary, a novel Z-scheme AgI/$Bi_{24}O_{31}Br_{10}$ 0D/2D heterojunction photocatalyst was successfully constructed by solvothermal and coprecipitation methods. The AB-30 composite possesses superior degradation efficiency of RhB (97.6%) under simulated sunlight irradiation, and its photodegradation rate constant k (0.029 min^{-1}) is approximately 20.7 and 2.9 times higher than that of

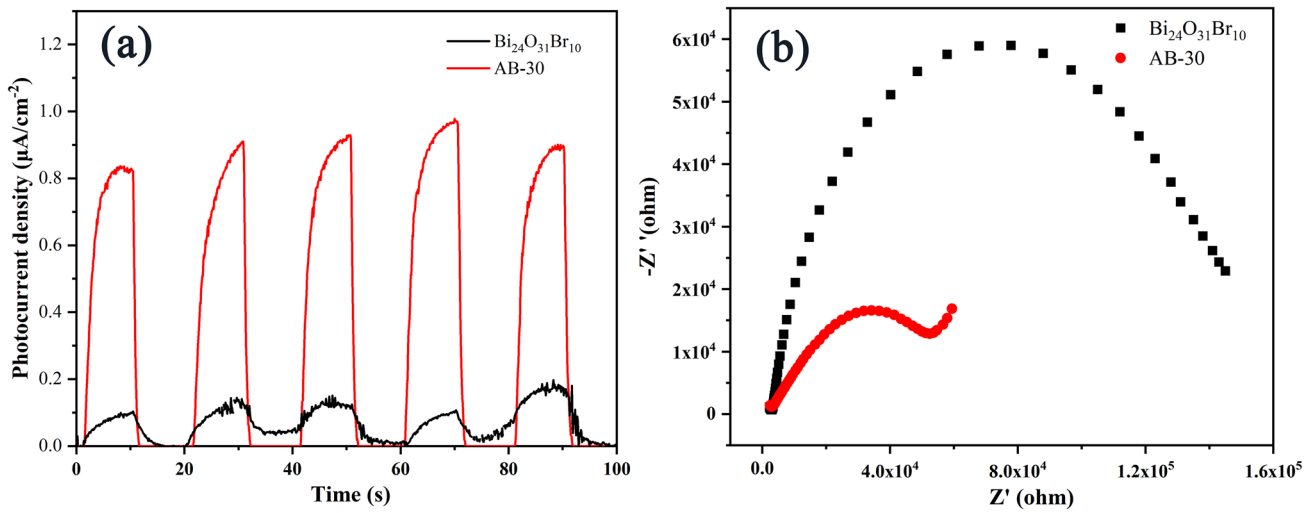

Fig. 12 **a** Photocurrent response and **b** EIS spectra of $Bi_{24}O_{31}Br_{10}$, AgI and AB-30 composite

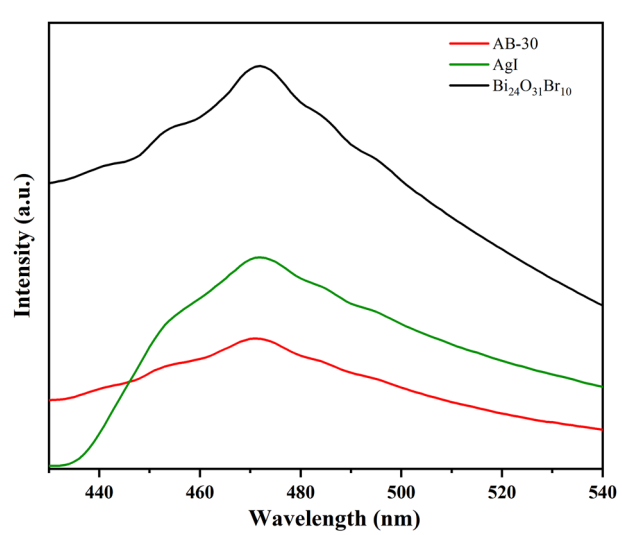

Fig. 13 PL spectra of $Bi_{24}O_{31}Br_{10}$, AgI and AB-30 samples

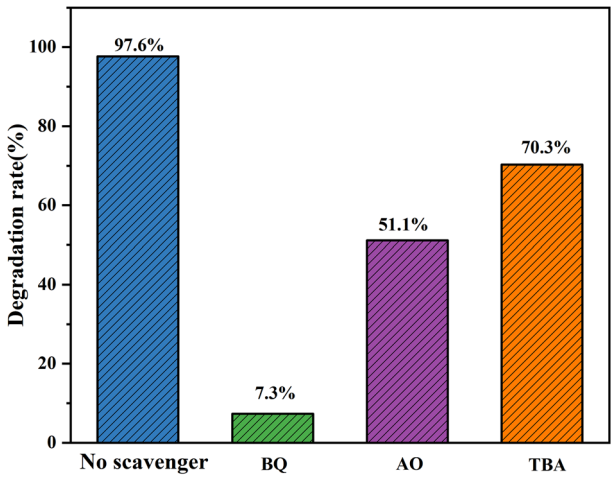

Fig. 14 Effects of various scavengers on the photocatalytic degradation of RhB over AB-30 composite

pure $Bi_{24}O_{31}Br_{10}$ (0.0013 min^{-1}) and AgI (0.010 min^{-1}), respectively. The improvement of photocatalytic efficiency is attributed to the following reasons: (a) The 0D/2D heterostructure of AgI/$Bi_{24}O_{31}Br_{10}$ composite has a larger specific surface area than that of $Bi_{24}O_{31}Br_{10}$, which could provide a large number of active sites and enhance its absorption of visible-light; (b) The effective separation of photo-excited charge carriers was benefitted from the unique Z-scheme carriers transfer pathway. In addition, AB composites exhibit relatively stable photocatalytic activity. This work provides a new strategy to enhance the photocatalytic activity of $Bi_{24}O_{31}Br_{10}$ via constructing the Z-scheme system for the treatment of organics degradation.

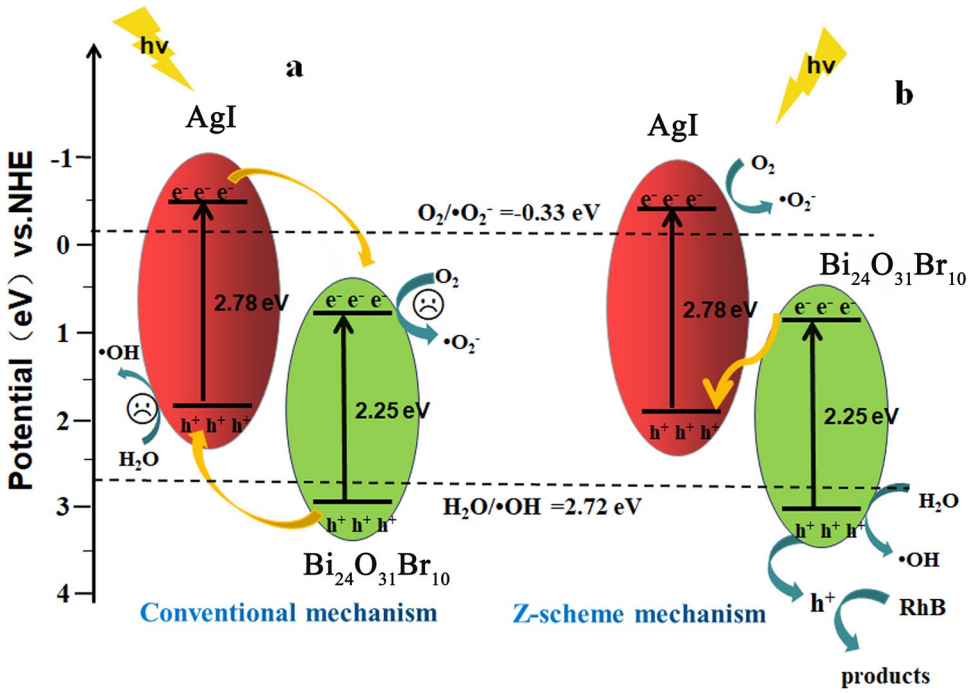

Fig. 15 Possible photocatalytic mechanisms for AgI/$Bi_{24}O_{31}Br_{10}$ composite

Acknowledgements This work was supported by the National Natural Science Foundation of China (Nos. 21076092, 21376099, 21546002, 21878115).

References

1. M.L. Marin, L. Santos-Juanes, A. Arques, A.M. Amat, M.A. Miranda, Chem. Rev. **112**, 1710 (2011)
2. X. Xu, C. Randorn, P. Efstathiou, J.T. Irvine, Nat. Mater. **11**, 595 (2012)
3. W. Xue, Z. Peng, D. Huang, G. Zeng, J. Wan, R. Xu, M. Cheng, C. Zhang, D. Jiang, Z. Hu, J. Hazard. Mater. **359**, 290 (2018)
4. F. Guo, W. Shi, H. Wang, M. Han, W. Guan, H. Huang, Y. Liu, Z. Kang, J. Hazard. Mater. **349**, 111 (2018)
5. X. Xiao, R. Hu, C. Liu, C. Xing, X. Zuo, J. Nan, L. Wang, Chem. Eng. J. **225**, 790 (2013)
6. D. Huang, Z. Li, G. Zeng, C. Zhou, W. Xue, X. Gong, X. Yan, S. Chen, W. Wang, M. Cheng, Appl. Catal. B: Environ. **240**, 153 (2019)
7. H. Li, J. Shang, Z. Ai, L. Zhang, J. Am. Chem. Soc. **137**, 6393 (2015)
8. L. Ye, Y. Su, X. Jin, H. Xie, C. Zhang, Environ. Sci. NANO **1**, 90 (2014)
9. G. Zhu, M. Hojamberdiev, S. Zhang, S.T.U. Din, W. Yang, Appl Surf Sci. **968**, 467 (2019)
10. Y. Chen, X. Ji, S. Vadivel, B. Paul, Ceram. Int. **44**, 23320 (2018)
11. J. Wang, L. Tang, G. Zeng, Y. Deng, H. Dong, Y. Liu, L. Wang, B. Peng, C. Zhang, F. Chen, Appl Catal B-environ. **115**, 222 (2018)
12. Y. Xing, D. Wu, X. Jin, J. Peng, Q. Yang, G. Ni, Solid State Sci. **105921**, 95 (2019)
13. C. Zhao, Z. Wang, X. Li, X. Yi, H. Chu, X. Chen, C. Wang, Chem. Eng. J. **123431**, 389 (2020)
14. Y. Cui, Q. Jia, H. Li, J. Han, L. Zhu, S. Li, Y. Zou, J. Yang, Appl. Surf. Sci. **290**, 233 (2014)
15. Y. Dai, P. Ren, Y. Li, D. Lv, Y. Shen, Y. Li, H. Niemantsverdriet, F. Besenbacher, H. Xiang, W. Hao, Angew. Chem. Int. Ed. **58**, 6265 (2019)
16. Z. Jiang, C. Xiao, X. Yin, L. Xu, C. Liu, H. Wang, Ceram. Int. **46**, 10771 (2020)
17. X. Chen, J. Zhang, L. Liu, B. Hu, Y. Zhao, S. Zhao, W. Zhao, S. Li, X. Hai, Appl. Surf. Sci. **491**, 1 (2019)
18. W. Wu, X. Ma, D. Li, Y. Xuan, S. Meng, M. Chen, J. Mater. Sci. **53**, 15804 (2018)
19. Y. Peng, P. Yu, Q. Chen, H. Zhou, A. Xu, J. Phys. Chem. C. **119**, 13032 (2015)
20. P. Zhou, J. Yu, M. Jaroniec, Adv. Mater. **26**, 4920 (2014)
21. Z. He, Y. Xia, J. Su, RSC Adv. **8**, 39187 (2018)
22. W. Xue, D. Huang, J. Li, G. Zeng, R. Deng, Y. Yang, S. Chen, Z. Li, X. Gong, B. Li, Chem. Eng. J. **373**, 1144 (2019)
23. F. Chen, Q. Yang, F. Yao, S. Wang, J. Sun, H. An, K. Yi, Y. Wang, Y. Zhou, L. Wang, J. Catal. **352**, 160 (2017)
24. W. Jiang, C. An, J. Liu, S. Wang, L. Zhao, W. Guo, J. Liu, Dalton T. **43**, 300 (2014)
25. Y. Yang, Z. Zeng, C. Zhang, D. Huang, G. Zeng, R. Xiao, C. Lai, C. Zhou, H. Guo, W. Xue, Chem. Eng. J. **349**, 808 (2018)
26. H. Yu, B. Huang, H. Wang, X. Yuan, L. Jiang, Z. Wu, J. Zhang, G. Zeng, J. Colloid Interf. Sci. **522**, 82 (2018)
27. W. Xue, Z. Peng, D. Huang, G. Zeng, X. Wen, R. Deng, Y. Yang, X. Yan, Ceram. Int. **45**, 6340 (2019)
28. J. Chen, X. Xiao, Y. Wang, M. Lu, X. Zeng, J. Alloys Compd. **5**, 88 (2019)
29. Q. Fang, B. Li, Y. Li, W. Huang, W. Peng, X. Fan, G. Huang, Adv. Powder Technol. **8**, 1576 (2019)
30. C. Wang, X. Zhang, H. Qiu, G. Huang, H. Yu, Appl. Catal. B: Environ. **205**, 615 (2017)
31. X. Yuan, Z. Wu, G. Zeng, L. Jiang, J. Zhang, T. Xiong, H. Wang, D. Mo, Appl. Surf. Sci. **454**, 293 (2018)
32. X. Wen, C. Niu, M. Ruan, L. Zhang, G. Zeng, J. Colloid Interf. Sci. **497**, 368 (2017)
33. J. Wang, Y. Yu, L. Zhang, Appl. Catal. B: Environ. **136**, 112 (2013)

34. Z. Ye, X. Xiao, J. Chen, Y. Wang, J. Photochem. Photobiol. A: Chem. **368**, 153 (2019)
35. H. Guo, C. Niu, L. Zhang, X. Wen, C. Liang, X. Zhang, D. Guan, N. Tang, G. Zeng, A.C.S. Sustain, Chem. Eng. **6**, 8003 (2018)
36. Z. Zhang, J.T. Yates Jr., Chem. Rev. **112**, 5520 (2012)
37. J. Shang, W. Hao, X. Lv, T. Wang, X. Wang, Y. Du, S. Dou, T. Xie, D. Wang, J. Wang, ACS Catal. **4**, 954 (2014)
38. S. Han, H. Liu, C. Sun, P. Jin, Y. Chen, J. Mater. Sci. **53**, 12030 (2018)
39. K. Vignesh, M. Kang, Mater. Sci. Egn.:B, **199**, 30(2015)
40. C. Zhang, H. Liu, W. Wang, H. Qian, S. Cheng, Y. Wang, Z. Zha, Y. Zhong, Y. Hu, Appl. Catal. B: Environ. **239**, 309 (2018)
41. Y. Li, K. Lv, W. Ho, F. Dong, X. Wu, Y. Xia, Appl. Catal. B: Environ. **202**, 611 (2017)
42. C. Zeng, Y. Hu, H. Huang, A.C.S. Sustain, Chem. Eng. **5**, 3897 (2017)
43. C. Zhou, C. Lai, D. Huang, G. Zeng, C. Zhang, M. Cheng, L. Hu, J. Wan, W. Xiong, M. Wen, Appl. Catal. B: Environ. **220**, 202 (2018)
44. X. Gao, X. Zhang, Y. Wang, S. Peng, B. Yue, C. Fan, Chem. Eng. J. **263**, 419 (2015)
45. F. Chen, H. Huang, C. Zeng, X. Du, Y. Zhang, A.C.S. Sustain, Chem. Eng. **5**, 7777 (2017)
46. W. Jiang, X. Zong, L. An, S. Hua, X. Miao, S. Luan, Y. Wen, F. Tao, Z. Sun, ACS Catal. **8**, 2209 (2018)